Apparent slip of shear thinning fluid in a microchannel with a superhydrophobic wall

Stanislav Patlazhan[1,2,*] and Sergei Vagner[2]

[1]*Semenov Institute of Chemical Physics of the Russian Academy of Sciences, 4 Kosygin Street, Moscow 119991, Russia*

[2]*Institute of Problems of Chemical Physics of the Russian Academy of Sciences, 1 Semenov Avenue, Chernogolovka, Moscow Region 142432, Russia*

(Received 4 February 2017; published 10 July 2017)

The peculiarities of simple shear flow of shear thinning fluids over a superhydrophobic wall consisting of a set of parallel gas-filled grooves and solid stripes (domains with slip and stick boundary conditions) are studied numerically. The Carreau-Yasuda model is used to provide further insight into the problem of the slip behavior of non-Newtonian fluids having a decreasing viscosity with a shear rate increase. This feature is demonstrated to cause a nonlinear velocity profile leading to the apparent slip. The corresponding transverse and longitudinal apparent slip lengths of a striped texture are found to be noticeably larger than the respective effective slip lengths of Newtonian liquids in microchannels of various thicknesses and surface fractions of the slip domains. The viscosity distribution of the shear thinning fluid over the superhydrophobic wall is carefully investigated to describe the mechanism of the apparent slip. Nonmonotonic behavior of the apparent slip length as a function of the applied shear rate is revealed. This important property of shear thinning fluids is considered to be sensitive to the steepness of the viscosity flow curve, thus providing a way to decrease considerably the flow resistance in microchannels.

DOI: 10.1103/PhysRevE.96.013104

I. INTRODUCTION

Microfluidic chips have found a variety of applications such as in biology, medicine and pharmaceutics, and environmental monitoring [1–4]. They consist of ensembles of microchannels transporting both homogeneous and multiphase fluid substances. Fluid flow in microchannels usually has a high hydrodynamic resistance, which may limit the fluid pump rate and can lead to undesirable deformations or even destruction of their walls. Reduction of the flow resistance is therefore one of the key issues in microfluidics. Until recently, in the creation of microfluidic devices attention was focused on hydrophobic inorganic or organic materials such as silica, PDMS, PMMA, PAA, and PC [5]. These materials enable lower friction due to a weak interaction of fluids with the channel walls. In the simplest case of Navier boundary conditions [6] the developed near-wall fluid velocity is proportional to the shear rate with

$$u_0 = l\left.\frac{\partial u}{\partial y}\right|_{y=0}, \tag{1}$$

where l is the local slip length. This fundamental characteristic corresponds to the distance between the fluid-solid interface and the point where the tangent of the velocity profile is extrapolated to 0. Although the slip length of a clean smooth hydrophobic surface is of the order of a few tens of nanometers [7–9], this effect becomes negligible in the velocity profile for channels having a distance between walls larger than 1 μm.

Superhydrophobic coatings allow a new approach to solving the drag reduction problem. They provide a significant increase in the slip length due to the existing specific microrelief allowing accumulation of gas bubbles in the pockets between the microscopic asperities (the Cassie-Baxter state) [10–12]. Classic examples of such surfaces are lotus leaves, cabbage, butterfly wings, and water striders. These are known for their extremely low wetting properties with contact angles exceeding 150° due to the restricted contacts with solid projections. The liquid freely moves on the fluid-gas interface. This motion may be treated as an apparent slip with an extrapolated length

$$l_{\text{app}} = \varepsilon\left(\frac{\eta}{\eta_\varepsilon} - 1\right) \tag{2}$$

by analogy to the two-layer system modeling a near-wall depletion layer ε whose viscosity η_ε is lower than the viscosity η of the basic medium [13,14]. At the fluid-gas interface, the apparent slip length varies from a few tens to hundreds of microns. The alternation of zones with slip and stick boundary conditions on the superhydrophobic coating results in an effective slip with a slip length considerably larger than that of the hydrophobic surface [15–18].

Theoretical studies and numerical simulations of the hydrodynamic properties of superhydrophobic surfaces available in the literature were carried out mainly for Newtonian fluids. In the case of a random or regular isotropic distribution of posts or holes, the effective Navier slip length was calculated as the ratio of the average value of the near-wall fluid velocity to the shear rate [19–21]. However, most studies have focused on anisotropic textures consisting of parallel grooves and ribs [15,16,19,22–30]. These superhydrophobic structures have attracted particular interest since they allow one to obtain accurate solutions for the velocity profiles and the effective slip lengths $l^N_{\text{eff},\parallel}$ and $l^N_{\text{eff},\perp}$ along and across stripes, which can then serve as standards for the analysis of numerical and experimental data. In particular, it was concluded from these particular cases that the principal effective slip lengths of Newtonian fluids do not exceed the period L of the superhydrophobic texture even for a large surface fraction φ of the grooves. In a deep channel with a thickness H larger than L, the longitudinal and transverse slip lengths become independent of H, while their ratio is approximately equal

*sapat@yandex.ru

to $l^N_{\text{eff},\parallel}/l^N_{\text{eff},\perp} \cong 2$ [16]. This equality is satisfied for a large local slip length, $l \geqslant 5L$, at the fluid-gas interface using an arbitrary value of φ [26]. On the contrary, for a shallow channel with a thickness H much smaller than the period L of the texture and local slip length l at the fluid-gas interface, we have $l^N_{\text{eff},\parallel}/l^N_{\text{eff},\perp} \cong 4$ [27].

So far, the effective slip length of Newtonian fluids has always been considered to depend only on the particular structure of the superhydrophobic surface and to be independent of the shear rate. However, molecular dynamics simulation revealed this shear rate dependence of the intrinsic slip on the hydrophobic surface [31]. This effect is conditioned by the low fluid-solid interaction energy and results in a sharp increase in the slip length at a given critical shear rate, being dependent on the molecular length scales and density of the solid substrate. In turn, the surface roughness was found to reduce this effect significantly [32]. The shear-rate-dependent slip of Newtonian fluids was confirmed experimentally on a smooth partly wetted solid surface [33] and it was shown that the measured slip length may increase up to a few microns with an increase in the shear rate. This effect was theoretically considered to be a consequence of the dynamic behavior of nanobubbles [34]. In the case of polymer melt shearing past atomically flat surfaces, molecular dynamics simulation shows that the slip length decreases slightly at low shear rates and then quickly increases at higher rates [35]. This nonmonotonic dependence on shear rate was shown to be caused by the nonlinear dependence of the fluid friction coefficient on the slip velocity.

The slip flow of an inelastic shear thinning fluid through a tube with a superhydrophobic wall containing transverse grooves and ribs has been studied numerically by Haase *et al.* [36] and showed the nonmonotonic dependence of the effective slip length on the pressure gradient. It was recognized that the abnormal behavior of the slip length is associated with large variations in the shear stress near the patterned wall, implying considerable changes in the viscosity of the non-Newtonian fluid. The influence of the protrusion angle θ of the fluid-gas interfaces was also investigated [36] and showed that the increase in the protrusion angle results in nonmonotonous behavior of the slip length with its maximum located closely to the flat interface ($\theta = 0$). It may lead to a small or even negative slip length, which is in qualitative agreement with similar results derived for Newtonian fluids [37–40].

In this study, we investigate numerically the peculiarities of simple shear flow of a shear thinning fluid past an anisotropic superhydrophobic texture with parallel stripes and grooves on the bottom wall of a microchannel. The main objective is to study the physical origin of the abnormal behavior of the apparent slip lengths both along and transverse to the texture axes. We found a notable depletion layer over the solid stripes, significantly reducing the near-wall effective viscosity of the shear thinning fluid and resulting in an increase in the apparent slip lengths. The shear-rate-dependent amplification of the apparent slip is shown to depend on the shape of the viscosity flow curve.

II. MODEL AND METHODS

The simple shear flow of incompressible Newtonian and shear thinning fluids is studied. It is generated between two

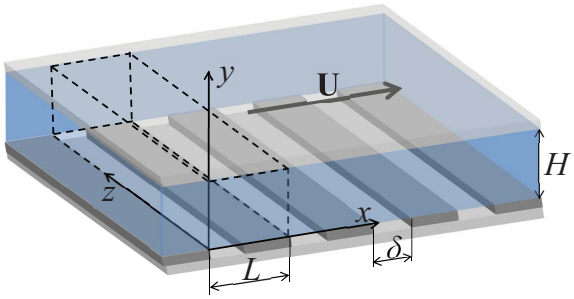

FIG. 1. Schematic of the superhydrophobic striped texture. Boundaries of the computational domain are represented by dashed lines.

parallel solid plates located a distance H from each other by the motion of the upper plate at a constant velocity $\mathbf{U}$. The bottom plate remains fixed. The basic shear rate $\dot{\gamma} = U/H$ is kept equal to 1 s^{-1} for any distance H between the walls (this choice is discussed in the final section, where the obtained results are generalized for a wider range of shear rates). The lower wall of the channel is covered by a superhydrophobic texture with a periodical set of parallel solid stripes and grooves of period L (see Fig. 1). The surface fraction of the grooves of width δ is equal to $\varphi = \delta/L$.

We suppose that the fluid does not penetrate into the grooves (Cassie-Baxter state) or protrude towards the fluid and that the fluid-gas interface is flat. This approximation was shown to be acceptable for small capillary numbers $\text{Ca} = \eta\dot{\gamma}\varphi L/\sigma$ and normal pressure. Under these conditions, the interface curvature can be ignored due to its small influence on the shear velocity profile [41,42]. However, the fluid depression may result in the protrusion of bubbles from the grooves, causing some undesirable effects as a decrease in the slip length [37,43]. This phenomenon is beyond the scope of our study. Nonetheless, for a shear thinning fluid, the dependence of the transverse slip length on the protrusion angle was found to be similar to that for a Newtonian fluid, varying only with the shear rate [36]. This suggests that the physical origin of the shear rate dependence for different slip lengths of a shear thinning fluid past a superhydrophobic texture (which is the main objective of this study) should not be noticeably affected by the protrusion angle of fluid-gas interfaces.

The hydrophilic upper wall of the microchannel is moving across or along the striped texture. As noted previously, the slip length at the solid parts of the texture is negligibly small compared to the slip length at the fluid-gas interface. Hence, the stick boundary condition was taken for the solid stripes, $\mathbf{u}_0 = 0$, while the perfect slip (or stress-free) boundary condition $\frac{\partial u}{\partial y}|_{y=0} = 0$ was imposed upon the fluid-gas interface. The velocity field $\mathbf{u}(x,y,z)$ in the channel was calculated from the Navier-Stokes equation along with the incompressibility condition,

$$\rho\left(\frac{\partial \mathbf{u}}{\partial t} + (\mathbf{u}\cdot\nabla)\mathbf{u}\right) = -\nabla p + \nabla\cdot\boldsymbol{\sigma} \quad \text{and} \quad \nabla\cdot\mathbf{u} = 0, \tag{3}$$

where ρ, p, and $\boldsymbol{\sigma}$ are the fluid density, pressure, and viscous stress tensor, respectively. Due to the translational symmetry of

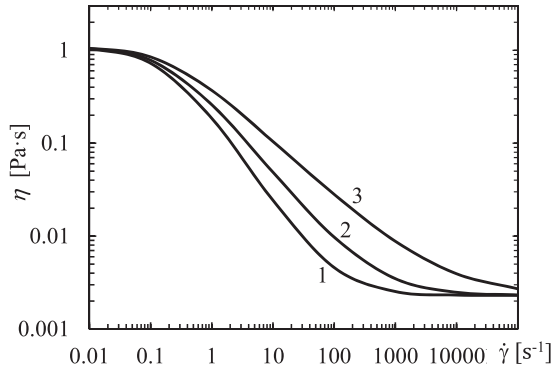

FIG. 2. Viscosity flow curves of the Carreau-Yasuda model for $\eta_0 = 1.08$ Pa s, $\eta_\infty = 0.0023$ Pa s, $\lambda = 5$ s, $a = 1$ and different n exponents: $n = 0.01$ (line 1), $n = 0.2$ (line 2), and $n = 0.4$ (line 3).

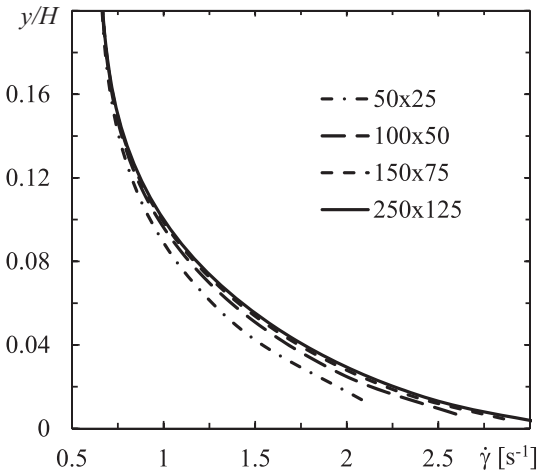

FIG. 3. Shear rate profiles calculated for different computational mesh sizes for a shear thinning fluid flowing in a microchannel with $H/L = 0.5$ across a superhydrophobic texture with $\varphi = 0.5$.

the superhydrophobic texture, calculation of the fluid velocity may be carried out within the computational domain including the solid strip and groove and obeying the periodic boundary conditions on its lateral sides. Under these conditions, the problem of shear flow across the texture is two-dimensional, while the problem of longitudinal flow must be addressed in three dimensions.

We study the flow behavior of an inelastic shear thinning fluid. Hence, the viscous stress tensor is defined as $\boldsymbol{\sigma} = \eta(J_2)\mathbf{D}$, where the fluid viscosity $\eta(J_2)$ is a function of the second invariant $J_2 \equiv \sum_{i,j} D_{ij} D_{ji}$ of the strain rate tensor $D_{ij} = \frac{1}{2}(\nabla_i u_j + \nabla_j u_i)$, with indices corresponding to axes x, y, and z of the laboratory coordinate system (Fig. 1). More particularly, for this non-Newtonian fluid, we consider the Carreau-Yasuda model, where the viscosity is determined as

$$\eta(J_2) = \eta_\infty + (\eta_0 - \eta_\infty)[1 + (2\lambda^2 J_2)^{\frac{a}{2}}]^{\frac{n-1}{a}}; \qquad (4)$$

here η_0 and η_∞ are the low and high shear rate viscosities, respectively; λ is the specific time; and the a and n exponents define the broadness of the shear thinning interval. If the upper wall moves along the x axis of the laboratory frame, then $J_2 = \frac{1}{2}\dot{\gamma}^2$ and Eq. (4) is transformed to the simple form

$$\eta(\dot{\gamma}) = \eta_\infty + (\eta_0 - \eta_\infty)[1 + (\lambda\dot{\gamma})^a]^{\frac{n-1}{a}}. \qquad (5)$$

This equation was used successfully to describe the velocity profiles of various shear thinning fluids such as blood and polymer solutions in microchannels [44–46]. Particularly, the viscosity flow curve of a 500-ppm aqueous solution of polyacrylamide in a microchannel is described by the following parameters: $\eta_0 = 1.08$ Pa s, $\eta_\infty = 0.0023$ Pa s, $\lambda = 5$ s, $a = 1$, and $n = 0.2$ [46] (see line 2 in Fig. 2).

It is seen that in the range of shear rates between 0.1 and 10^3 s^{-1} the viscosity declines steadily, while at $\dot{\gamma} \leqslant 0.01$ s^{-1} and $\dot{\gamma} \geqslant 10^4$ s^{-1} the fluid viscosity approaches the upper and lower Newtonian plateaus with viscosities of 1.08 and 0.0023 Pa s, respectively. Therefore, the previously considered basic shear rate $\dot{\gamma} = 1$ s^{-1} lies within the shear thinning range. For this reason, any fluctuations in shear rate will cause perturbations of the viscosity. As described below, this feature determines the specifics of the hydrodynamic behavior of a shear thinning fluid in the vicinity of a superhydrophobic coating. Figure 2 includes also the viscosity flow curves with different n exponents. This demonstrates that the decrease in n results in a steeper reduction in viscosity with an increase in shear rate. The impact of this effect on the slippage of shear thinning fluids past a superhydrophobic coating is discussed in the last section.

Note that for the stripe texture with groove surface fraction $\varphi = 0.5$ and the given range of shear rates of the shear thinning fluids (see Fig. 2), the corresponding capillary numbers $\mathrm{Ca} = \eta\dot{\gamma}\varphi L/\sigma$ are located between 1.4×10^{-2} and 7.1×10^{-6}, thus ensuring that the curvature of the fluid-gas interfaces is small at the normal pressure [41,42].

The numerical solutions of Eqs. (3) and (4) were carried out using the OpenFoam package [47]. The solutions of the Navier-Stokes equations for an incompressible fluid were obtained by means of the finite-volume method [48], based on a sampling of the integral form of the original Eqs. (3) at each control volume. This ensures the conservation of mass and momentum on the discrete level. The control volumes can take any shape and have a different number of adjacent cells that can meet the challenges in a computational domain of arbitrary complexity. One of the specifics of the numerical simulation of the incompressible fluid flow is the lack of an explicit equation for the pressure. To solve this problem, the PISO (pressure implicit with splitting of operator) method was employed.

To determine the optimal homogeneous orthogonal computational mesh, the convergence of solutions obtained for different mesh sizes was investigated. The shear rate profiles and the corresponding apparent slip lengths $l^P_{\mathrm{app},\perp}$ (see Sec. III, below) were calculated for the considered aqueous solution of polyacrylamide in a microchannel for a simple shear flow across the symmetric striped texture with a period $L = 100$ μm, a slip area fraction $\varphi = 0.5$, and a microchannel thickness $H = 50$ μm. The results are presented in Fig. 3 and Table I. We can observe that the shear rate profiles and the effective Navier slip lengths converge to their limits on the mesh with 250×125 cells in the (x, y) plane of the computational domain shown in Fig. 1. Hence, all results presented below were calculated on this mesh.

TABLE I. Apparent slip lengths for different mesh sizes.

	Mesh size				
	50 × 25	100 × 50	150 × 75	200 × 100	250 × 125
$l^P_{\text{app},\perp}$	0.282	0.280	0.278	0.274	0.274

III. RESULTS AND DISCUSSION

A. Effective and apparent slip lengths of Newtonian and shear thinning fluids

Figure 4 presents the mean velocity profiles of a Newtonian liquid with a viscosity $\eta_0 = 1.08$ Pa s along with a shear thinning 500-ppm aqueous solution of polyacrylamide obeying the Carreau-Yasuda model (Fig. 2). They were calculated for a simple shear flow along and across a stripe superhydrophobic texture with $\varphi = 0.5$ in a microchannel with a unit nondimensional thickness ($H/L = 1$). It is shown that for the Newtonian fluid, the velocity varies linearly and reveals a slip both along and across the stripes. The corresponding effective slip lengths $l^N_{\text{eff},\parallel}$ and $l^N_{\text{eff},\perp}$ are given by the segments between $y = 0$ and the intersections of the lines with the y axis.

On the other hand, the velocity profiles of the shear thinning fluid show a qualitatively different behavior: the mean velocity changes linearly just away from the bottom wall but its gradient increases a short distance from the superhydrophobic texture. This kind of velocity distribution resembles the flow behavior of a two-layer fluid with a low-viscosity near-wall layer promoting the apparent slip. The observed nonzero velocity at the bottom wall (Fig. 4, curves 1 and 2) may be caused by an additional slip of the virtual low-viscosity layer. As a result, Eq. (2) is invalid in the case of the shear thinning fluid for the apparent slip length. The physical mechanism of this behavior is discussed in the next section. Extrapolation of the linear parts of the mean velocity profiles of the shear thinning fluid up to the intersection with the y axis gives the apparent slip

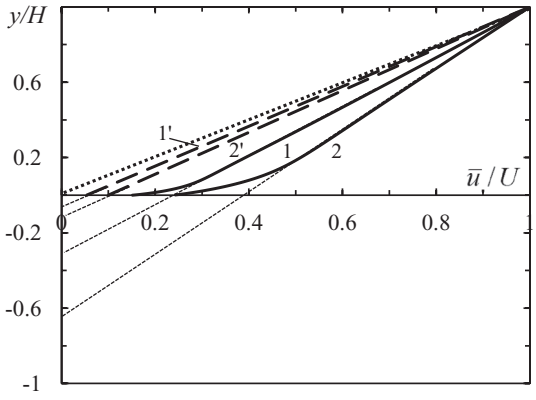

FIG. 4. Mean velocity profiles of Newtonian (bold dashed lines) and Carreau-Yasuda shear thinning fluids (bold solid lines) across (1,1′) and along (2,2′) the symmetric superhydrophobic coating with $\varphi = 0.5$ in a channel with $H/L = 1$. The bold dotted line represents the velocity profile at $\varphi = 0$ and basic shear rate $\dot{\gamma} = 1\ \text{s}^{-1}$. Extrapolation of the linear parts of the mean velocity profiles of the shear thinning fluid (thin dotted lines).

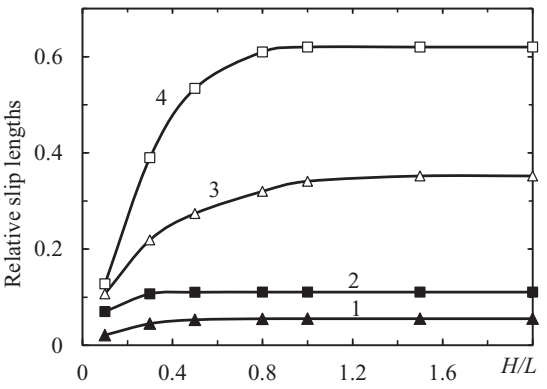

FIG. 5. Dependence of the transverse and longitudinal effective and apparent slip lengths of Newtonian and shear thinning fluids on the relative thickness of the microchannel at a surface fraction of grooves $\varphi = 0.5$: $l^N_{\text{eff},\perp}/L$ (curve 1), $l^N_{\text{eff},\parallel}/L$ (curve 2), $l^P_{\text{app},\perp}/L$ (curve 3), and $l^P_{\text{app},\parallel}/L$ (curve 4).

lengths $l^P_{\text{app},\parallel}$ and $l^P_{\text{app},\perp}$ along and across the striped texture (the superscript P denotes the polymeric fluid). As follows from Fig. 4, these characteristics are significantly larger than the corresponding effective slip length of a Newtonian fluid.

The dependences of the effective and apparent slip lengths of the Newtonian and shear thinning fluids on the relative microchannel thickness H/L are shown in Fig. 5 for a simple shear flow along and across the symmetric texture. For the Newtonian liquid, the calculated curves coincide with the corresponding analytical solutions [16,49]. More specifically, the numerical simulations result in the relation $l^N_{\text{eff},\parallel} \simeq 2l^N_{\text{eff},\perp}$, which satisfies the known theoretical solution derived under the condition that the local slip length l at the fluid-gas interface is much larger than the period L of the striped texture [16]. On the other hand, the apparent slip lengths $l^P_{\text{app},\parallel}$ and $l^P_{\text{app},\perp}$ of the shear thinning fluid are several times larger than the corresponding effective slip lengths $l^N_{\text{eff},\parallel}$ and $l^N_{\text{eff},\perp}$ of the Newtonian fluid for any channel thickness. We observe that for the considered shear thinning fluid, the relation $l^P_{\text{app},\parallel} \simeq 1.88 l^P_{\text{app},\perp}$ takes place, which differs from that for the Newtonian liquid. The effective and apparent slip lengths of both fluids reach saturation at $H \geqslant L$. Also, the saturation of the longitudinal and transverse apparent slip lengths occurs at larger values of H for the shear thinning fluid compared to the Newtonian one. Indeed, in the first case, the threshold thickness of the microchannel is of the order of $H_c \sim L$, while for a Newtonian fluid H_c is somewhat lower.

Figure 6 shows that an increase in the surface fraction φ of the gas-filled zones in a striped superhydrophobic wall leads to significant growth of the effective and apparent slip lengths. The obtained numerical solutions for the effective slip length of the Newtonian fluid across the texture are in agreement with the known theoretical result $l^N_{\text{eff},\perp} = \frac{L}{2\pi} \ln[\cos^{-1}(\frac{\pi\varphi}{2})]$ derived at $l \gg L$ [16]. However, this relationship does not hold for the shear thinning fluid. Figure 6 indicates that the growth of φ results in a faster increase in the apparent slip lengths $l^P_{\text{app},\parallel}$ and $l^P_{\text{app},\perp}$ compared to the similar pair $l^N_{\text{eff},\parallel}$ and $l^N_{\text{eff},\perp}$ for the Newtonian fluid. Indeed, the ratio of the apparent transverse slip lengths calculated at $\varphi = 0.5$ and $\varphi = 0.75$

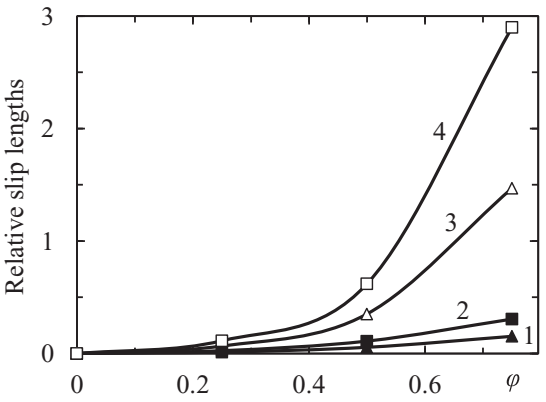

FIG. 6. Dependence of the transverse and longitudinal effective and apparent slip lengths of Newtonian and shear thinning fluids on the surface fraction of grooves of the striped superhydrophobic texture in a microchannel of relative thickness $H/L = 1.5$: $l^N_{\text{eff},\perp}/L$ (curve 1), $l^N_{\text{eff},\parallel}/L$ (curve 2), $l^P_{\text{app},\perp}/L$ (curve 3), and $l^P_{\text{app},\parallel}/L$ (curve 4).

shows that $l^P_{\text{app},\perp}(0.75)/l^P_{\text{app},\perp}(0.5) \simeq 4.2$ for the shear thinning fluid, whereas for the Newtonian fluid this ratio is noticeably lower, i.e., $l^N_{\text{eff},\perp}(0.75)/l^N_{\text{eff},\perp}(0.5) \simeq 2.8$.

B. Shear-induced structure of a shear thinning fluid over a striped texture

To understand the origin of the differences in the effective and apparent slip lengths of Newtonian versus shear thinning fluids, it should be taken into account that the alternation of stripes with the slip and stick boundary conditions on the superhydrophobic texture results in shear rate disturbances in the microchannel. For a Newtonian fluid it has been found that the perturbations of flow rate $\mathbf{u}' = \mathbf{u} - \langle \mathbf{u} \rangle$ are rather sensitive to the channel thickness as well as the surface fraction φ of the grooves [50]. In a wide channel ($H/L \geqslant 1$), the perturbations are located near the superhydrophobic wall, whereas for a ratio of $H/L < 1$, the velocity perturbations capture the entire space between the walls. On the other hand, an increase in φ leads to an increase in $\mathbf{u}'$. The disturbances in the flow velocity are linked to the perturbations of shear rate. Figure 7 shows profiles of the relative shear rates of a shear thinning fluid in the central sections over domains with slip ($x = L/4$) and stick ($x = 3L/4$) boundary conditions of a striped texture with $\varphi = 0.5$ (cf. Fig. 1). To make the applied shear rate $\dot{\gamma}$ dimensionless as a function of the type of fluid and flow direction, the unit shear rate $\dot{\gamma}_{\text{unit}}$ was defined as one of the following values: $\dot{\gamma}_{\text{eff},\perp} = U/(H + l^N_{\text{eff},\perp})$, $\dot{\gamma}_{\text{eff},\parallel} = U/(H + l^N_{\text{eff},\parallel})$ or $\dot{\gamma}_{\text{app},\perp} = U/(H + l^P_{\text{app},\perp})$, $\dot{\gamma}_{\text{app},\parallel} = U/(H + l^P_{\text{app},\parallel})$. In Fig. 7, the shear rate drops to 0 at the fluid-gas interface (in accordance with the stress-free boundary condition), while, by contrast, the local shear rate increases considerably in the vicinity of the stick area. This is caused by a sharp decrease in the fluid velocity at the solid stripes.

Comparison of the Newtonian liquid over the solid stripes with the shear rate profile (dotted lines) shows a much stronger perturbation of the shear rate of the shear thinning fluid in this domain. Nevertheless, their corresponding profiles are almost

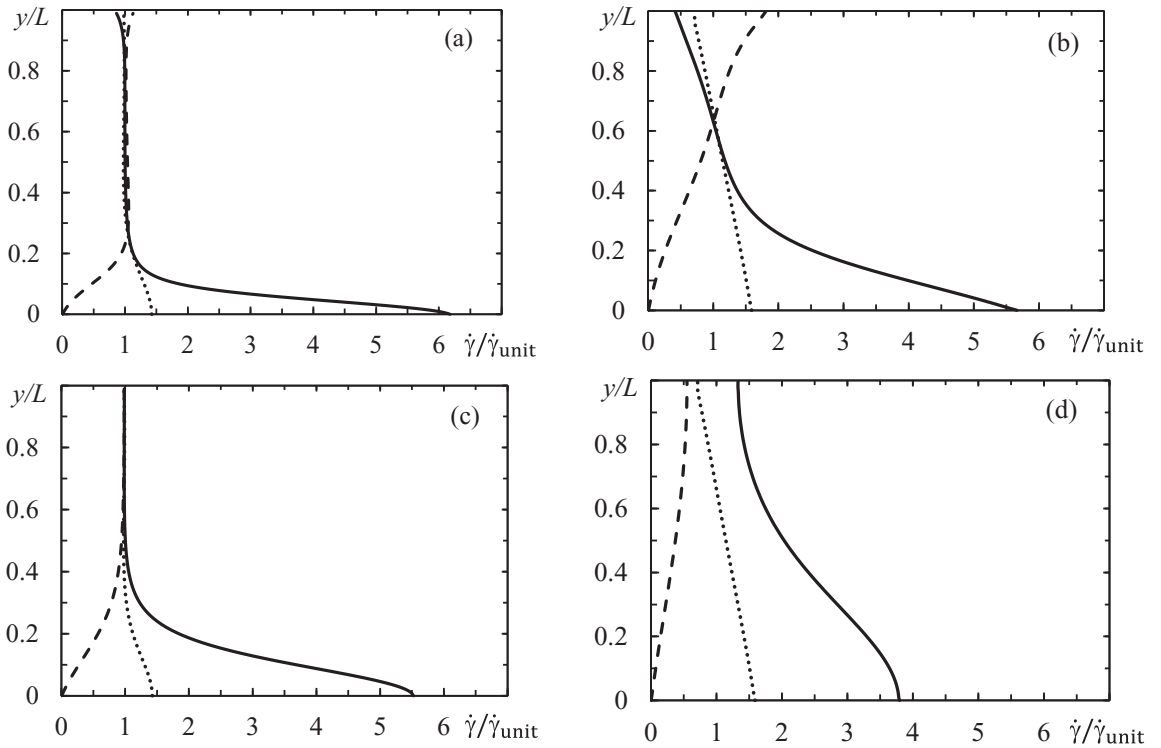

FIG. 7. Shear rate profiles of the shear thinning fluid in the central sections of the slip ($x = 0.25L$; dashed line) and stick ($x = 0.75L$; solid line) areas of the symmetric striped texture $\varphi = 0.5$ under transverse (a, b) and longitudinal (c, d) shear flow in microchannels of different thicknesses: $H/L = 1$ (a, c) and $H/L = 0.3$ (b, d). Dotted lines represent the corresponding shear rate profiles of the Newtonian fluid in the central section of the stick area.

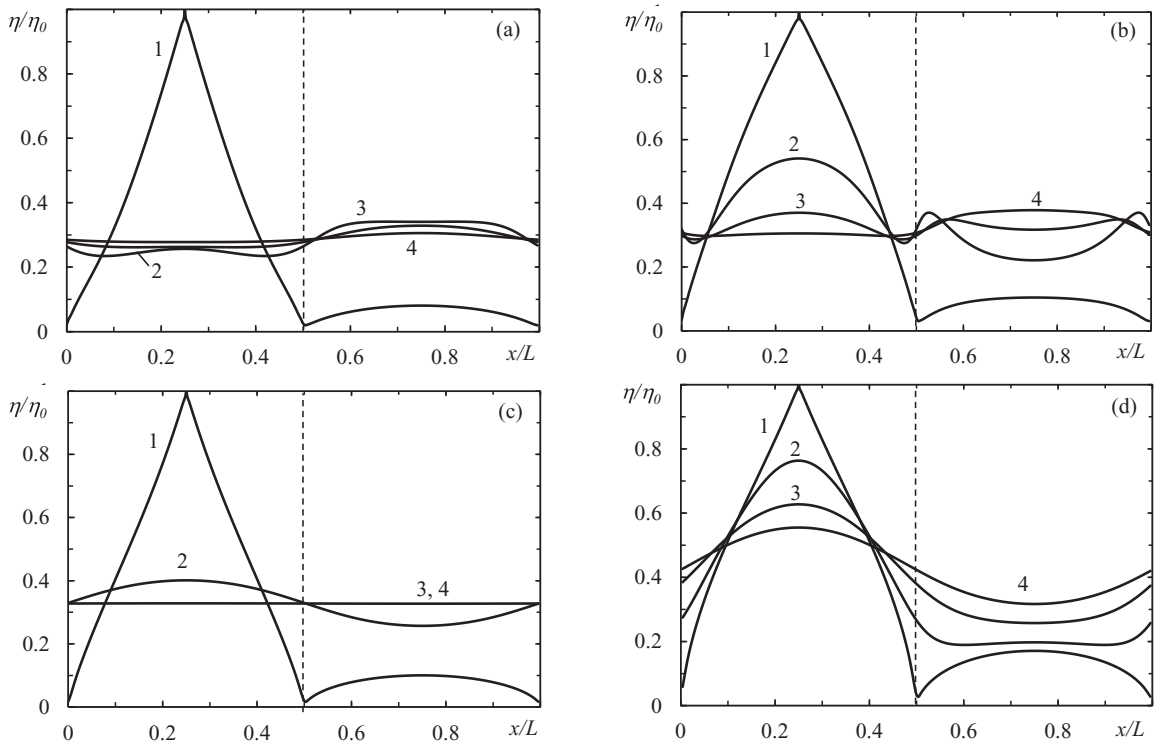

FIG. 8. Variation of the relative viscosity of a shear thinning fluid across a striped texture with $\varphi = 0.5$ at different distances—$y/H = 0$ (curve 1), $y/H = 0.25$ (curve 2), $y/H = 0.5$ (curve 3), and $y/H = 0.75$ (4)—from the bottom wall under transverse (a, b) and longitudinal (c, d) simple shear flow in microchannels with different thicknesses, $H/L = 1$ (a, c) and $H/L = 0.3$ (b, d). The dotted vertical line separates the slip and stick areas of the calculation domain.

identical over the fluid-gas interface. Just as in the case of a Newtonian fluid, the perturbations of the shear rate of the shear thinning fluid in the wide channel ($H/L \geqslant 1$) are localized in a narrow zone near the superhydrophobic wall. On the contrary, when $H/L < 1$, the perturbations extend deep into the microchannel for both transverse and longitudinal flows [cf. Figs. 7(a) vs 7(b) and 7(c) vs 7(d)].

Figure 8 shows the variations of the relative viscosities of a fluid across a symmetric striped texture with $\varphi = 0.5$ under transverse [Figs. 8(a) and 8(b)] and longitudinal [Figs. 8(c) and 8(d)] simple shear flow at different distances y from the bottom wall of microchannels with relative thicknesses $H/L = 0.3$ and 1.0. As can be observed, in both cases, the viscosity of the shear thinning fluid increases drastically over the slip sections, reaching a maximum in the center of the zone (curve 1). On the contrary, the viscosity decreases markedly over the solid stripes. This occurs when $\dot{\gamma}/\dot{\gamma}_{\text{unit}} > 1$ in agreement with Fig. 7 (solid curves). Over the solid stripes, the viscosity variations of the shear thinning fluid almost disappear when moving away from the superhydrophobic coating (see Fig. 8, curves 2 and 3). For the basic shear rate $\dot{\gamma} = 1\ \text{s}^{-1}$, the viscosity is stabilized at $\eta \simeq 0.3\eta_0$ in a channel of thickness $H/L \geqslant 1$ [Figs. 8(a) and 8(c), curve 4]. In contrast, in narrow channels for $H/L < 1$, the area of viscosity perturbation expands. This is especially noticeable for a longitudinal flow [Fig. 8(d), curves 2–4]. These effects are consistent with the behavior of local shear rates presented in Fig. 7: the increase or decrease in the viscosity of the shear thinning fluid over the gas-filled grooves and solid stripes, respectively, is associated with the fall or rise of the shear rate over the corresponding areas.

To analyze the viscosity distribution of a shear thinning fluid along the vertical y axis, we looked at the viscosities preaveraged along the x coordinate over the slip and stick areas, $\overline{\eta}_{\text{slip}}(y) = \frac{2}{L}\int_0^{L/2} \eta(x,y)dx$ and $\overline{\eta}_{\text{stick}}(y) = \frac{2}{L}\int_{L/2}^{L} \eta(x,y)dx$. The results are shown in Fig. 9 for a superhydrophobic texture with groove fraction $\varphi = 0.5$ and different microchannel thicknesses. It can be seen that the relative viscosity $\overline{\eta}_{\text{stick}}(y)/\eta_0$ falls drastically when close to the superhydrophobic wall, while $\overline{\eta}_{\text{slip}}(y)/\eta_0$ increases, which is consistent with the behavior of the local viscosities shown in Fig. 8. When $H/L \geqslant 1$, the main variations in the viscosities are localized in the narrow vicinity of the superhydrophobic wall [see Figs. 9(a) and 9(c)]. This layer is slightly wider for the longitudinal shear flow compared to the transverse flow. On the contrary, in a narrow channel with $H/L < 1$, perturbations of the preaveraged viscosities near the bottom wall and away from it are of the same amplitude [Figs. 9(b) and 9(d)], which is due to the deeper penetration of the shear rate perturbations inside the channel [cf. Figs. 7(b) and 7(d)]. If these results are compared with the behavior of the effective ($l^N_{\text{eff},\parallel}$ and $l^N_{\text{eff},\perp}$) and apparent ($l^P_{\text{app},\parallel}$ and $l^P_{\text{app},\perp}$) slip lengths of the Newtonian and shear thinning fluids shown in Fig. 5, we can conclude that the reduction in the slip lengths at $H/L < 1$ is associated with the perturbations of the shear rates.

Figure 10 shows the influence of the groove surface fraction φ on a modification of the shear-induced viscous structure of a non-Newtonian fluid for transverse and longitudinal flow over

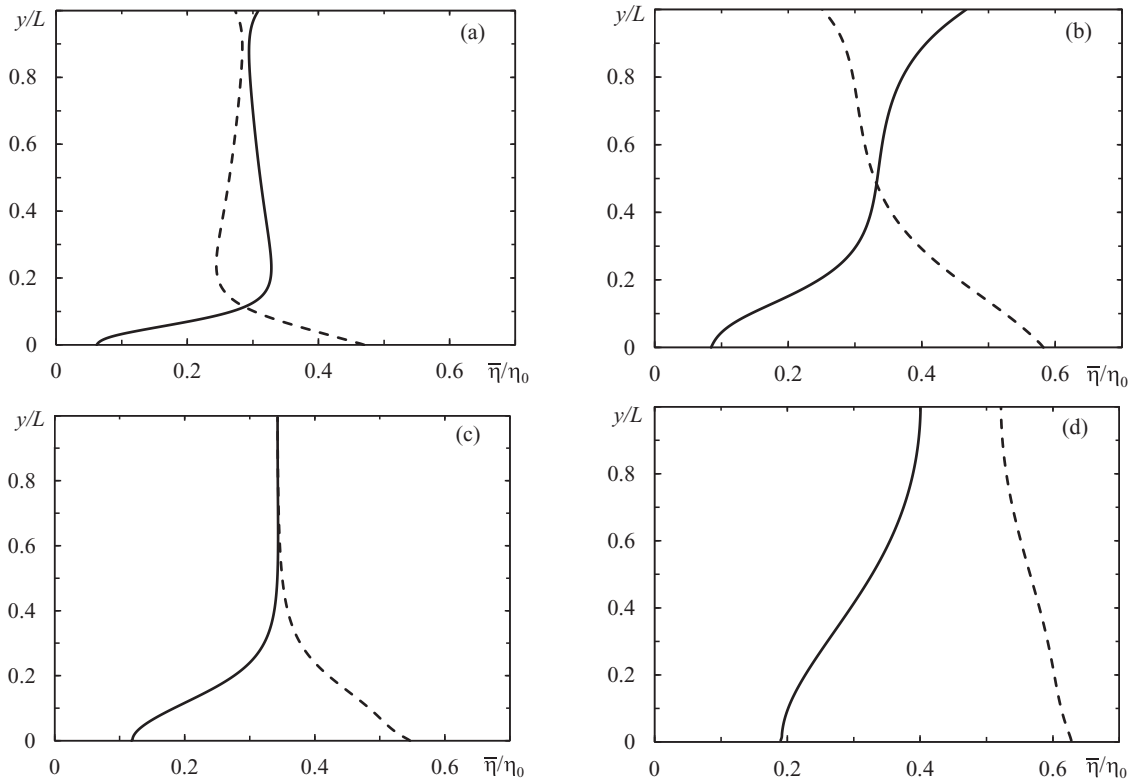

FIG. 9. Distribution of the relative preaveraged viscosities $\overline{\eta}_{\rm slip}(y)/\eta_0$ (dashed lines) and $\overline{\eta}_{\rm stick}(y)/\eta_0$ (solid lines) over the striped texture with $\varphi = 0.5$ under transverse (a, b) and longitudinal (c, d) simple shear flow in microchannels with relative thicknesses $H/L = 1$ (a, c) and $H/L = 0.3$ (b, d).

striped textures with $\varphi = 0.25$ and $\varphi = 0.75$. It can be seen that a decrease in φ results in a reduction of the preaveraged viscosities $\overline{\eta}_{\rm slip}(y)/\eta_0$ and $\overline{\eta}_{\rm stick}(y)/\eta_0$ in the upper part of the channel, while an increase in φ leads to a shift of the curves towards higher viscosities. The changes in the preaveraged viscosities are correlated with the dependence of the apparent slip lengths $l^P_{\rm app,\parallel}$ and $l^P_{\rm app,\perp}$ on the surface fraction of the grooves (see Fig. 6). A decrease in φ results in a reduction in the slip lengths, causing an increase in the average shear rates and, consequently, a reduction in the viscosity of the shear thinning fluid according to Eq. (5). In addition, the viscosity drops near the solid stripes (see Fig. 10, curve 2) while it increases over the grooves (see Fig. 10, curve 1). On the other hand, the growth of φ leads to an increase in the viscosity perturbations through the depth of the channel (Fig. 10, curves 3 and 4).

The results indicate that the near-wall layer of the shear thinning fluid over the superhydrophobic texture is highly heterogeneous and consists in a periodic sequence of high- and low-viscosity domains (see Figs. 8–10). This impacts particularly the preaveraged local velocity profiles $\overline{u}_{\rm stick}(y) = \frac{2}{L}\int_{L/2}^{L} u(x,y)dx$ and $\overline{u}_{\rm slip}(y) = \frac{2}{L}\int_{0}^{L/2} u(x,y)dx$ of the transverse shear flow over the solid stripes and gas-filled grooves at $\varphi = 0.5$ and $H/L = 1$ presented in Fig. 11(a) by curves 1 and 2, respectively. The preaveraged velocity $\overline{u}_{\rm stick}(y)$ over the stick area decreases gradually to 0, while $\overline{u}_{\rm slip}(y)$ is nonzero at the fluid-gas interface, thus indicating a local slip. Superposition of the preaveraged velocities gives the mean velocity profile $\overline{u}(y) = \frac{1}{2}(\overline{u}_{\rm slip} + \overline{u}_{\rm stick}) = \frac{1}{L}\int_0^L u(x,y)dx$, which is represented by curve 3 in Fig. 11(a) (cf. Fig. 4, curve 1).

The distortion of the mean velocity profile indicates the existence of a near-wall layer (ε layer) with an average viscosity $\overline{\eta}_\varepsilon$ lower than the $\overline{\eta}_C$ of the overlying medium. This layer undergoes slip past the superhydrophobic coating. The velocity profile is linear above the ε layer and its approximation to the intersection with the y axis gives the apparent slip length. For comparison, Fig. 11(b) shows the distribution of the preaveraged velocities $\overline{u}_{\rm slip}(y)$ and $\overline{u}_{\rm stick}(y)$ over the grooves (curve 1) and solid stripes (curve 2) of the texture together with the mean velocity profile $\overline{u}(y)$ (line 3) of the sheared Newtonian fluid of viscosity η_0. For this case, in contrast to the shear thinning fluid, the mean velocity is a linear function up to the intersection with the bottom wall, which corresponds to the effective Navier slip.

C. Mechanism of the apparent slip of a shear thinning fluid

Figure 12(a) shows the relative viscosity field $\eta(x,y)/\eta_0$ of a Carreau-Yasuda fluid under the basic shear rate $\dot{\gamma} = 1\ {\rm s}^{-1}$ across a symmetric texture with $\varphi = 0.5$ in a microchannel with a relative thickness $H/L = 1$. Dark areas correspond to a high viscosity, while light areas represent domains with a low viscosity. This viscosity field is in agreement with Fig. 8(a), showing the viscosity variations of a shear thinning fluid. The strongly inhomogeneous near-wall layer, with high and low viscosities over the slipping and sticking areas, is clearly

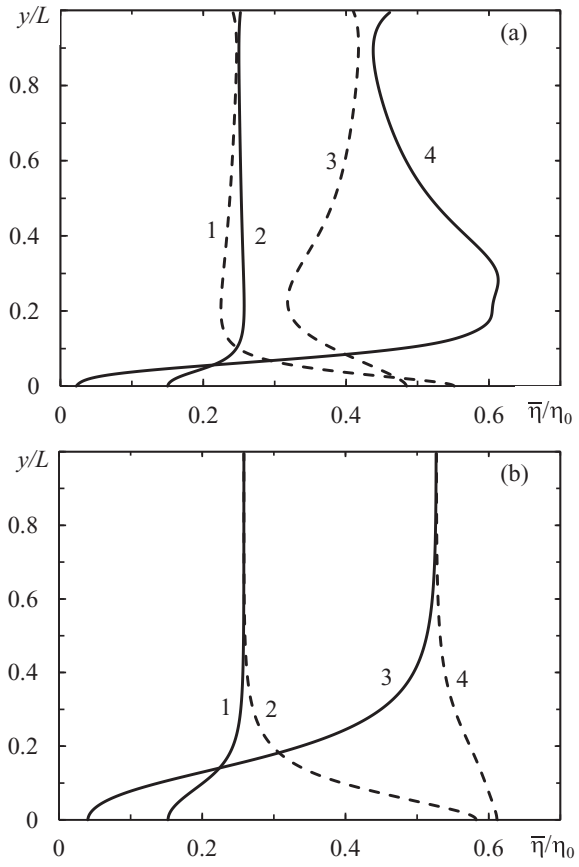

FIG. 10. Distribution of the preaveraged relative viscosities $\overline{\eta}_{\text{slip}}(y)/\eta_0$ (dashed lines) and $\overline{\eta}_{\text{stick}}(y)/\eta_0$ (solid lines) over striped textures with $\varphi = 0.25$ (curves 1 and 2) and $\varphi = 0.75$ (curves 3 and 4) under transverse (a) and longitudinal (b) simple shear flow in microchannels of relative thickness $H/L = 1$.

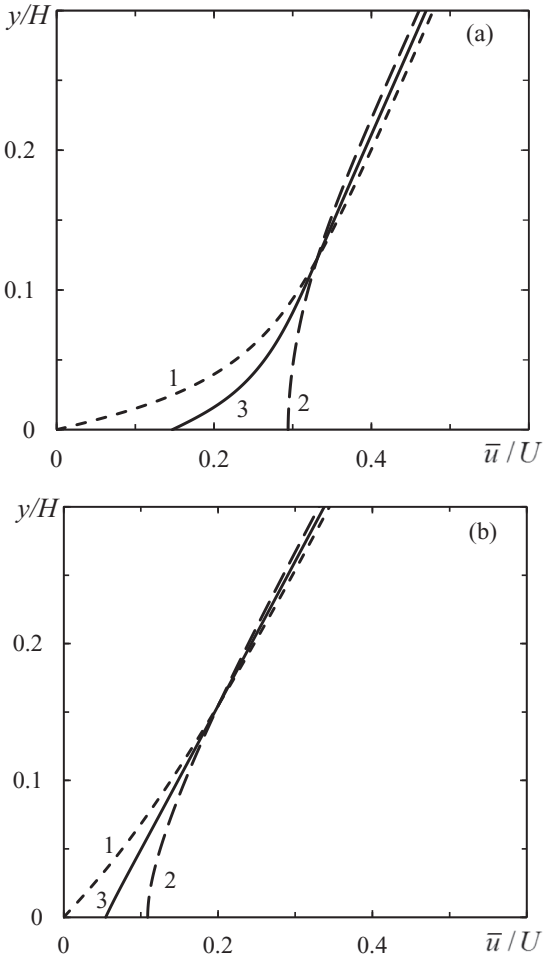

FIG. 11. Preaveraged $\overline{u}_{\text{stick}}$ and $\overline{u}_{\text{slip}}$ (curves 1 and 2) and mean $\overline{u}$ (curve 3) velocity profiles of shear thinning (a) and Newtonian (b) fluids sheared across the striped texture with $\varphi = 0.5$ in a microchannel of $H/L = 1$.

visible. The perturbations of viscosity in the upper part of the channel are much weaker for the specified thickness.

We consider an approximate model taking into account the observed viscous distribution to show that such a viscosity distribution is the main reason for the apparent slip of a shear thinning fluid past the superhydrophobic texture. To this end, we select three zones within the computational domain: (i) the near-wall areas A and B, of the same thickness, abutted against grooves and solid stripes, respectively; and (ii) the distant domain C, located above [see Fig. 12(b)]. The thickness ε of the selected domains A and B is taken to be equal to the distance from the superhydrophobic wall to the intersection point of the corresponding average velocity profiles over the slip and stick areas [Fig. 11(a)]. Viscosities of the A, B, and C domains are taken equal to the corresponding mean values, which are estimated as the average viscosities of stratified systems flowing along the layers: $\eta_A = \frac{2\varepsilon}{L}(\int_0^{\varepsilon}(\int_0^{L/2}\eta(x,y)dx)^{-1}dy)^{-1}$, $\eta_B = \frac{2\varepsilon}{L}(\int_0^{\varepsilon}(\int_{L/2}^{L}\eta(x,y)dx)^{-1}dy)^{-1}$, and $\eta_C = \frac{H-\varepsilon}{L}(\int_{\varepsilon}^{H}(\int_0^{L}\eta(x,y)dx)^{-1}dy)^{-1}$. Figure 9(a) provides the following relations between these mean viscosities of the selected domains: $\eta_B < \eta_C < \eta_A$.

The simplified configuration of the mean viscosity field presented in Fig. 12(b) allows us to estimate the average shear rate in the A and B domains as $\dot{\gamma}_A = u_\varepsilon/(\varepsilon + l)$ and $\dot{\gamma}_B = u_\varepsilon/\varepsilon$; l is the local slip length of domain A, and u_ε is the velocity at the outer border of the ε layer. The viscous stresses in the A and B domains are $\sigma_A = \eta_A\dot{\gamma}_A$ and $\sigma_B = \eta_B\dot{\gamma}_B$. The macroscopic average shear rate and viscous stresses are defined as $\dot{\gamma}_\varepsilon = \varphi\dot{\gamma}_A + (1-\varphi)\dot{\gamma}_B$ and $\sigma_\varepsilon = \varphi\sigma_A + (1-\varphi)\sigma_B$, respectively. They represent the hydrodynamic characteristics of a homogenized ε-layer boundary [Fig. 12(c)] and their relationship $\sigma_\varepsilon = \eta_\varepsilon\dot{\gamma}_\varepsilon$ determines the effective viscosity of the ε layer as

$$\eta_\varepsilon = \frac{\varphi\eta_A\varepsilon + (1-\varphi)\eta_B(\varepsilon + l)}{\varepsilon + l(1-\varphi)}. \tag{6}$$

In the considered case of a perfect local slip, $l \to \infty$, Eq. (6) gives $\eta_\varepsilon = \eta_B$. This means that the effective viscosity of the ε layer is of the order of the average viscosity of zone B located over the sticking area. This is the lowest local viscosity of the shear thinning fluid over the striped texture and provides the necessary condition for the occurrence of the apparent slip. On the other hand, unlike in the classical case [see Eq. (2)], the ε layer undergoes slip. The corresponding effective Navier slip

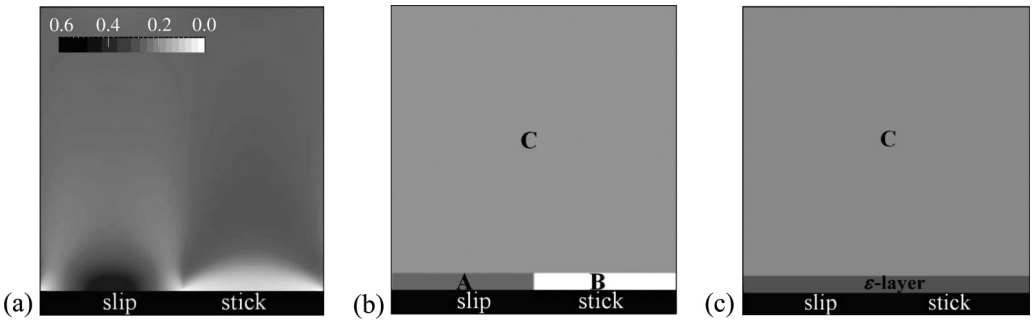

FIG. 12. Relative viscosity field $\eta(x,y)/\eta_0$ of a shear thinning fluid under simple shear flow across the superhydrophobic striped texture with $\varphi = 0.5$ at $H/L = 1$: (a) result of the numerical calculations; (b) averaged viscosities in the A, B, and C domains; (c) averaged two-layer structure.

length l_ε of the ε layer can therefore be estimated from the comparison of the above definition of the average shear rate with the relationship $\dot{\gamma}_\varepsilon = u_\varepsilon(\varepsilon + l_\varepsilon)^{-1}$ and gives

$$l_\varepsilon = \frac{\varphi\varepsilon l}{\varepsilon + l(1-\varphi)}. \tag{7}$$

In the limit of the perfect slip ($l \to \infty$) the effective slip length is equal to $l_\varepsilon = \varphi(1-\varphi)^{-1}\varepsilon$ and an increase in the groove surface fraction results in an increase in l_ε as it should.

To estimate the apparent slip length $l_{\rm app}$, the flow velocity profile $u_C(y)$ in the upper layer, C, is determined by the ratio $u_C = U(y + l_{\rm app})(H + l_{\rm app})^{-1}$. Here, the flow velocity at the upper border of the ε-layer is equal to $u_\varepsilon = U(\varepsilon + l_{\rm app})(H + l_{\rm app})^{-1}$. Taking into account the continuity of the viscous stresses at the interface between domain C and the ε layer as well as the definition of the shear rate $\dot{\gamma}_\varepsilon$ in the ε layer, we obtain the required apparent slip length of the shear thinning fluid past the striped superhydrophobic wall:

$$l_{\rm app} = \varepsilon\left(\frac{\eta_C}{\eta_\varepsilon} - 1\right) + \frac{\eta_C}{\eta_\varepsilon} l_\varepsilon. \tag{8}$$

The first term in Eq. (8) is similar to Eq. (2) for the apparent slip length of Newtonian fluids, while the second one represents the contribution of the effective Navier slip of the ε layer. The last term is found to increase the apparent slip length of the shear thinning fluid [cf. Eq. (2)]. Substitution of Eq. (7) into Eq. (8) gives

$$l_{\rm app} = \varepsilon\left(\frac{\eta_C}{\eta_\varepsilon}\frac{\varepsilon + l}{\varepsilon + (1-\varphi)l} - 1\right), \tag{9}$$

which, for a perfect slip at the fluid-gas interface, becomes

$$l_{\rm app} = \varepsilon\left[\frac{\eta_C}{\eta_\varepsilon}(1-\varphi)^{-1} - 1\right]. \tag{10}$$

In the case of a symmetric texture with $\varphi = 0.5$, this gives $l_{\rm app} = \varepsilon(2\frac{\eta_C}{\eta_\varepsilon} - 1)$. Hence, Eqs. (8)–(10) indicate that at a given fraction of the slip areas of the superhydrophobic wall, the magnitude of the apparent slip length of the shear thinning fluid is governed by the ratio η_C/η_ε of the mean viscosities of the C domain and ε layer.

A comparison of the transverse apparent slip lengths $l^P_{{\rm app},\perp}$ calculated numerically with those estimated from Eqs. (6) and (9) at different fractions of the slip areas is shown in Fig. 13. It can be seen that the rough estimates of the apparent transverse slip length almost coincide with the results of the numerical simulation for $\varphi = 0.25$ and 0.5, whereas at $\varphi = 0.75$ they are only qualitatively consistent. This is due to the fact that the simplified representation of the ε layer corresponds better to the local viscosity distribution at $\varphi \leqslant 0.5$ [cf. Figs. 9(a) and 10(a)]. However, at $\varphi = 0.75$ the viscosity disturbances in the upper part of the channel become comparable to those in the vicinity of the striped texture [see Fig. 10(a), curves 3 and 4]. This leads to degeneration of the ε layer and thus increases the inaccuracies of the estimates. The same holds true for narrow channels of thickness $H < L$ when the viscosity perturbations are not localized near the superhydrophobic wall, making the simplified model inappropriate [cf. Fig. 9(b)]. Nevertheless, even in this case, the estimated apparent slip length remains valid qualitatively. Hence, it may be concluded that the viscosity variations near the superhydrophobic wall provide the major contribution to the nonlinear behavior of the velocity profiles of the shear thinning fluids (see Fig. 4). The same mechanism of apparent slip is valid for the longitudinal flow. The only difference is that the viscosity perturbations in the vicinity of the superhydrophobic texture in this case are larger than those in the transverse flow, while the perturbations rapidly decay away from the bottom wall [see Fig. 9(c)].

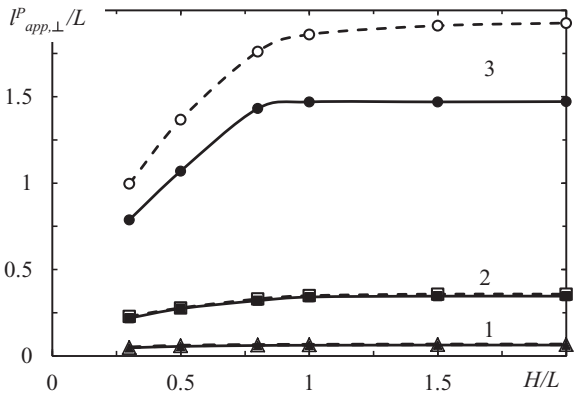

FIG. 13. Comparison of the behavior of the apparent transverse slip lengths of the shear thinning fluid obtained by numerical simulation (solid lines) and from Eqs. (6)–(9) (dashed lines) in microchannels with superhydrophobic coating of different fractions of grooves: $\varphi = 0.25$ (curve 1), $\varphi = 0.5$ (curve 2), and $\varphi = 0.75$ (curve 3).

Also, the angular displacement Θ of the stripe superhydrophobic texture relative to the flow direction may result in the generation of a secondary helicoidal flow favoring the mixture of fluids [51–53]. For Newtonian fluids, the corresponding slip length $l^N_{\mathrm{eff},\Theta}$ was shown to match the known expression $l^N_{\mathrm{eff},\Theta} = l^N_{\mathrm{eff},\perp}\cos^2\Theta + l^N_{\mathrm{eff},\parallel}\sin^2\Theta$, thus confirming the concept of a tensorial effective slip [54,55]. Our numerical calculations also confirmed this result. However, for the non-Newtonian shear thinning fluid, we found a deviation of the numerically estimated apparent slip length from the equation $l^P_{\mathrm{app},\Theta} = l^P_{\mathrm{app},\perp}\cos^2\Theta + l^P_{\mathrm{app},\parallel}\sin^2\Theta$, indicating a violation of the tensor form of the apparent slip. The indirect evidence of this inference is the large difference in the helical flow periods of the Newtonian versus shear thinning fluids over the same superhydrophobic stripe textures [52,53], which is caused by the formation of the mentioned near-wall depletion layer in the latter case. This issue would require a more detailed study.

D. Shear rate dependence of the apparent slip length

The mechanism of the apparent slip discussed above is triggered when the basic shear rate falls within the range of the viscosity decrease of the non-Newtonian fluid (see Fig. 2). It results in a multidirectional variation of the local viscosities over the fluid-gas interfaces and solid stripes due to the free motion and slowing-down of the fluid, respectively, thus engendering a low-viscosity boundary layer. So far, we have considered the hydrodynamic phenomena at a given shear rate $\dot\gamma = 1\ \mathrm{s}^{-1}$. The apparent slip lengths at this shear rate were shown to reach the highest levels when the microchannel thickness H is equal to or larger than the period L of the striped texture (see Fig. 5). In this case, the ratio of the transversal apparent slip length of a 500-ppm aqueous solution of polyacrylamide to that of a solution of pure water is equal to $l^P_{\mathrm{app},\perp}/l^N_{\mathrm{eff},\perp} \simeq 6.38$. This raises the question whether we can get larger slip lengths. For this, we examined the effect of shear rate on the apparent slip length, which, quantitatively, should also depend on the rate of viscosity reduction controlled by the exponent n in the Carreau-Yasuda model [see Eqs. (2) and (4)].

Figure 14 shows the dependence of the apparent transverse slip lengths $l^P_{\mathrm{app},\perp}$ on the applied shear rate $\dot\gamma$ at $n = 0.01$, 0.2, and 0.4 in a microchannel with relative thickness $H/L = 1$ and a striped superhydrophobic texture with $\varphi = 0.5$. It follows that $l^P_{\mathrm{app},\perp}(\dot\gamma)$ is a nonmonotonic function. The magnitude and location of the maximum slip length are rather sensitive to the value of n. More specifically, the decrease in n is shown to cause (i) a increase in the maximum $l^{\max,P}_{\mathrm{app},\perp}$ of the slip length and (ii) a shift of the corresponding shear rate $\dot\gamma_{\max}$ towards smaller values.

Table II reports a sharp increase in the relative slip length $l^{\max P}_{\mathrm{app},\perp}/l^N_{\mathrm{eff},\perp}$ at $n = 0.01$ in comparison with larger values of n. This highlights the prospects of inelastic shear thinning fluids with sharp variation of viscosity flow curves for considerable drag reduction.

The origin of the nonmonotonic behavior of the apparent slip length with the shear rate is associated with the viscosity distribution in the microchannel. According to Eq. (10), the apparent slip length of the shear thinning fluid is governed by the ratio of the average viscosities η_C and η_ε in the C domain and ε layer defined above [Fig. 12(c)]. Figure 15 shows the variation of the viscosities with the shear rate. The increase in shear rate results in a faster decrease in the ε-layer viscosity η_ε than in the viscosity η_C in the C domain. A decrease in n leads to a sharper drop of η_ε with $\dot\gamma$, while it virtually does not influence the behavior of $\eta_C(\dot\gamma)$. As a result, the viscosity ratio η_C/η_ε becomes a nonmonotonic function of the shear rate. This is shown in the inset in Fig. 15.

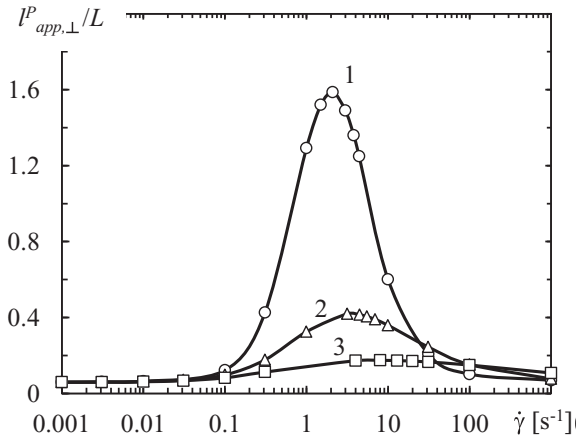

FIG. 14. Variations of the relative apparent transverse slip length $l^P_{\mathrm{app},\perp}/L$ with the basic shear rate in a microchannel with relative thickness $H/L = 1$ and striped texture with $\varphi = 0.5$ for $n = 0.01$ (curve 1), $n = 0.2$ (curve 2), and $n = 0.4$ (curve 3).

At low and high shear rates corresponding to the upper and lower Newtonian plateau of the Carreau-Yasuda fluid, both the viscosity ratio and the apparent slip length take the smallest values (cf. Figs. 14 and 15). The latter one confirms the early result about the weak dependence of the effective slip length of Newtonian fluids on their viscosity [15,16,26]. On the other hand, the maximum of the viscosity ratio η_C/η_ε increases promptly with a decrease in the exponent n, thus leading to an increase in the apparent slip length in accordance with Eq. (10). The shear rates $\dot\gamma_{\max}$ corresponding to the maximum of η_C/η_ε at different values of n coincide with those of the apparent slip length derived independently from the velocity profiles (see Fig. 4). These data provide additional support that the apparent slip length is attained due to the viscosity perturbations of the shear thinning fluid near the superhydrophobic wall.

It is noteworthy that the shear rate $\dot\gamma_{\max}$ at the maximum of the apparent slip correlates with the position of the inflection point $\dot\gamma_{\mathrm{inflect}}$ of the viscosity flow curve where the inclination of the curve is maximal (see Fig. 2). A decrease in the exponent n results in a decrease in both shear rates $\dot\gamma_{\max}$ and $\dot\gamma_{\mathrm{inflect}}$ (see Table II). Thus, one can conclude that the lowest drag

TABLE II. Dependence of slip characteristics on the exponent n.

	n		
	0.01	0.2	0.4
$l^{\max,P}_{\mathrm{app},\perp}/l^N_{\mathrm{eff},\perp}$	28.78	7.60	3.15
$\dot\gamma_{\max}$ (s^{-1})	2.10	3.16	8.00
$\dot\gamma_{\mathrm{inflect}}$ (s^{-1})	4.43	6.95	12.99

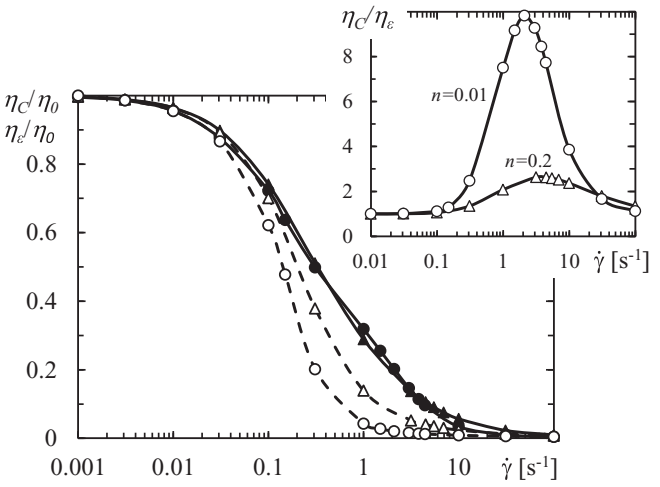

FIG. 15. Dependence of relative average viscosities η_C/η_0 (solid lines, filled symbols) and η_ε/η_0 (dashed lines, open symbols) of the C domain and ε layer on the basic shear rate $\dot\gamma$ in a microchannel with $H/L = 1$ and striped texture with $\varphi = 0.5$ for $n = 0.01$ (open and filled circles) and $n = 0.2$ (open and filled triangles). Inset: Variation of the viscosity ratio η_C/η_ε with the shear rate.

resistance in microchannels with superhydrophobic coating can be achieved with the shear thinning fluids having the steepest drop in the viscosity flow curve with shear rate.

IV. CONCLUSION

In summary, we have studied the peculiarities of slip behavior of shear thinning fluids in microchannels past a striped superhydrophobic texture. Using the Carreau-Yasuda model, we found that the origin of the slip flow of non-Newtonian fluids qualitatively differs from that of Newtonian fluids. The slip of shear thinning fluids is associated with the formation of a heterogeneous near-wall layer whose effective viscosity is much lower than that of the upper part of the channel. This depletion effect changes the average velocity profile of the shear thinning fluid, leading to the apparent slip. The resulting transverse and longitudinal apparent slip lengths are considerably larger than the effective Navier slip lengths of Newtonian fluids past the same superhydrophobic texture. The slip behavior of the shear thinning fluid is governed by the ratio of the effective viscosity of the near-wall depletion layer to that of the upper domain.

The apparent slip length is a nonmonotonic function of the shear rate. The position of its maximum corresponds to the shear rate located close to the inflection point of the viscosity flow curve. The increase in the curve steepness (due to the reduction of exponent n in the Carreau-Yasuda model) leads to a considerable increase in the apparent slip length. This important property of the shear thinning fluid was found to arise due to a corresponding decrease in the effective viscosity of the near-wall layer and may be used for notable drag reduction of microchannels.

ACKNOWLEDGMENTS

The authors wish to thank Dr. D. George of ICube, University of Strasbourg, France, for helpful discussions. The numerical calculations in this work were carried out using the computing resources of the Joint Supercomputer Center of the Russian Academy of Sciences.

[1] D. Mark, S. Haeberle, G. Roth, F. von Stetten, and R. Zengerle, Chem. Soc. Rev. **39**, 1153 (2010).
[2] J. P. Rothstein, Annu. Rev. Fluid Mech. **42**, 89 (2010).
[3] T. P. Lagus and J. Edd, J. Phys. D: Appl. Phys. **46**, 114005 (2013).
[4] E. K. Sackmann, A. L. Fulton, and D. J. Beebe, Nature **507**, 181 (2014).
[5] K. Ren, J. Zhou, and H. Wu, Acc. Chem. Res. **46**, 2396 (2013).
[6] C. L. M. H. Navier, Mem. Acad. R. Sci. Inst. France **6**, 389 (1823).
[7] J. L. Barrat and L. Bocquet, Phys. Rev. Lett. **82**, 4671 (1999).
[8] C. Cottin-Bizonne, B. Cross, A. Steinberger, and E. Charlaix, Phys. Rev. Lett. **94**, 056102 (2005).
[9] O. I. Vinogradova, K. Koynov, A. Best, and F. Feuillebois, Phys. Rev. Lett. **102**, 118302 (2009).
[10] R. J. Daniello, N. E. Waterhouse, and J. P. Rothstein, Phys. Fluids **21**, 085102 (2009).
[11] E. J. C. Barbier and B. D'Urso, arXiv:1406.0787 [physics.flu-dyn].
[12] T. Jung, H. Choi, and J. Kim, J. Fluid Mech. **790**, R1 (2016).
[13] H. A. Barnes, Non-Newton. Fluid Mech. **56**, 221 (1995).
[14] O. I. Vinogradova, Langmuir **11**, 2213 (1995).
[15] J. R. Philip and Z. Angew, Math. Phys. **23**, 960 (1972).
[16] E. Lauga and H. Stone, J. Fluid Mech. **489**, 55 (2003).
[17] P. Joseph, C. Cottin-Bizonne, J. M. Benoît, C. Ybert, C. Journet, P. Tabeling, and L. Bocquet, Phys. Rev. Lett. **97**, 156104 (2006).
[18] J. Li, M. Zhou, X. Ye, and L. Cai, J. Micromech. Microeng. **20**, 115022 (2010).
[19] Y. P. Cheng, C. J. Teo, and B. C. Khoo, Phys. Fluids **21**, 122004 (2009).
[20] A. M. J. Davis and E. Lauga, J. Fluid Mech. **661**, 402 (2010).
[21] C. Kunert, J. Harting, and O. I. Vinogradova, Phys. Rev. Lett. **105**, 016001 (2010).
[22] C. Y. Wang, Phys. Fluids **15**, 1114 (2003).
[23] C. Cottin-Bizonne, C. Barentin, E. Charlaix, L. Bocquet, and J.-L. Barrat, Eur. Phys. J. E **15**, 427 (2004).
[24] M. Sbragaglia and A. Prosperetti, Phys. Fluids **19**, 043603 (2007).
[25] C. J. Teo and B. C. Khoo, Microfluid. Nanofluid. **7**, 353 (2009).
[26] A. V. Belyaev and O. I. Vinogradova, J. Fluid Mech. **652**, 489 (2010).
[27] S. Schmieschek, A. V. Belyaev, J. Harting, and O. I. Vinogradova, Phys. Rev. E **85**, 016324 (2012).
[28] E. S. Asmolov and O. I. Vinogradova, J. Fluid Mech. **706**, 108 (2012).
[29] E. S. Asmolov, J. Zhou, F. Schmid, and O. I. Vinogradova, Phys. Rev. E **88**, 023004 (2013).

[30] T. V. Nizkaya, E. S. Asmolov, and O. I. Vinogradova, Phys. Rev. E **90**, 043017 (2014).
[31] P. A. Thompson and S. M. Troian, Nature (London) **389**, 360 (1997).
[32] A. Niavarani and N. V. Priezjev, Phys. Rev. E **81**, 011606 (2010).
[33] Y. Zhu and S. Granick, Phys. Rev. Lett. **87**, 096105 (2001).
[34] E. Lauga and M. P. Brenner, Phys. Rev. E **70**, 026311 (2004).
[35] A. Niavarani and N. V. Priezjev, Phys. Rev. E **77**, 041606 (2008).
[36] A. S. Haase, J. A. Wood, L. M. J. Sprakel, and R. G. H. Lammertink, Phys. Rev. E **95**, 023105 (2017).
[37] A. Steinberger, C. Cottin-Bizonne, P. Kleimann, and E. Charlaix, Nat. Mater. **6**, 665 (2007).
[38] J. Hyvaluoma and J. Harting, Phys. Rev. Lett. **100**, 246001 (2008).
[39] C. Teo and B. Khoo, Microfluid. Nanofluid. **17**, 891 (2014).
[40] Y. Xue, P. Lv, Y. Liu, Y. Shi, H. Lin, and H. Duan, Phys. Fluids **27**, 092003 (2015).
[41] J. Ou, B. Perot, and J. P. Rothstein, Phys. Fluids **16**, 4635 (2004).
[42] J. Ou and J. Rothstein, Phys. Fluids **17**, 103606 (2005).
[43] E. Karataya, A. Haase, C. Visserb, C. Sunb, D. Lohseb, P. Tsaia, and R. Lammertink, Proc. Natl. Acad. Sci. USA **110**, 8422 (2013).
[44] F. Abraham, M. Behr, and M. Heinkenschloss, Comput. Methods Biomech. Biomed. Eng. **8**, 127 (2005).
[45] J. Boyd, J. M. Buick, and S. Green, Phys. Fluids **19**, 093103 (2007).
[46] C. M. Bălan and C. Bălan, U.P.B. Sci. Bull. Series D **72**, 121 (2010).
[47] H. G. Weller, G. Tabor, H. Jasak, and C. Fureby, Comput. Phys. **12**, 620 (1998).
[48] M. Schäfer, *Computational Engineering—Introduction to Numerical Methods* (Springer-Verlag, Berlin, 2006), p. 321.
[49] E. S. Asmolov, A. V. Belyaev, and O. I. Vinogradova, Phys. Rev. E **84**, 026330 (2011).
[50] S. A. Vagner and S. A. Patlazhan, Doklady Phys. Chem. **459**, 203 (2014).
[51] J. Ou, G. R. Moss, and J. P. Rothstein, Phys. Rev. E **76**, 016304 (2007).
[52] D. Broboana, N. O. Tanase, and C. Balan, J. Non-Newton. Fluid Mech. **222**, 151 (2015).
[53] S. Vagner and S. A. Patlazhan, J. Phys.: Conf. Ser. **774**, 012027 (2016).
[54] K. Kamrin, M. Z. Bazant, and H. A. Stone, J. Fluid Mech. **658**, 409 (2010).
[55] J. Zhou, A. V. Belyaev, F. Schmid, and O. I. Vinogradova, J. Chem. Phys. **136**, 194706 (2012).